RESEARCH ARTICLE

CrossMark

Graphene–carbon nanotube hybrid catalyst layer architecture for reversible oxygen electrodes in rechargeable metal–air batteries
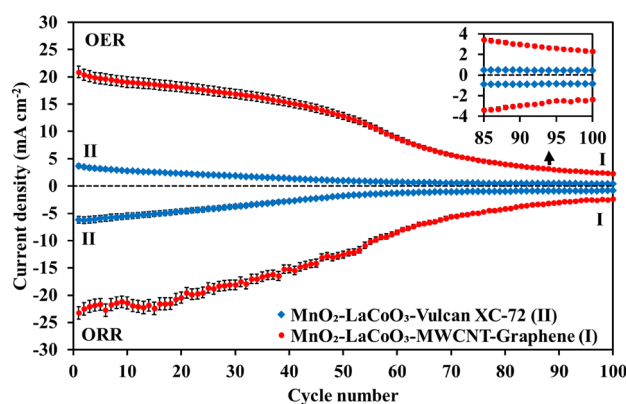
Miguel A. Garcia-Contreras[1,2] · Pooya Hosseini-Benhangi[1,3] · Előd L. Gyenge[1]

Abstract

Reversible oxygen reduction/evolution reaction (ORR/OER) electrodes with non-precious metal catalysts are essential for the larger scale development of rechargeable metal–air batteries and regenerative fuel cells. Here, an investigation of the catalyst layer morphology is presented with respect to the bifunctional ORR/OER activity and durability of MnO_2–$LaCoO_3$ catalyst in 6 M KOH. Graphene, N-doped graphene and multi-walled carbon nanotubes (MWCNT), alone and in combination, were studied as catalyst layer support. The graphene and N-doped graphene microsheets were prepared by ionic liquid-assisted electrochemical exfoliation of graphite. It was found that the hybrid support composed of graphene and MWCNT (1:1 wt) generated up to an order of magnitude higher ORR and OER current densities for MnO_2–$LaCoO_3$, compared to either graphene or MWCNT supports individually. The 3D scaffold-like architecture of the graphene microsheets and MWCNT pillars enhances the catalyst layer utilization efficiency and also improves the catalyst anchoring. The latter effects, together with the lower rates of carbon corrosion in the OER region and peroxide generation in the ORR region on the graphene-based supports compared to the reference Vulcan XC-72, contribute to the improved activity of the hybrid catalyst layer as demonstrated using accelerated potential deep cycle experiments.

Graphical abstract

Keywords Oxygen reduction and evolution reactions · Electrocatalysis · Catalyst support · Non-precious metal catalyst

---

Miguel A. Garcia-Contreras and Pooya Hosseini-Benhangi have contributed equally to this work.

Extended author information available on the last page of the article

1 Introduction

The reversible electrocatalysis of the oxygen reduction (ORR) and evolution reactions (OER) is essential for electrochemical power sources such as rechargeable metal–air batteries and regenerative fuel cells [1–6]. Typical ORR

🖄 Springer

and OER catalysts are noble metals and their oxides such as Pt, Ag, Ir, IrO_2, RuO_2 [2, 7–17]. Non-precious group metals (non-PGMs) and their oxides are the alternative, cost-effective, solution for next-generation catalyst materials. For separately ORR or OER in alkaline media, certain non-PGM catalysts demonstrated similar (or superior) activity and longer-term stability compared to noble metal catalysts. For example, in case of ORR, bimetallic (Fe,Mn)/N-doped carbon catalyst was shown to have three times higher initial activity and favorable stability compared to Pt/C, whereas for OER, nickel phosphate (4 $NiHPO_4 \cdot Ni_3(PO_4)_2 \cdot 22\ H_2O$) exhibited lower onset potential and Tafel slope compared to 20 wt% Ir/C coupled with superior durability during extended potential cycling [4–6, 13, 14, 18, 19].

The bifunctional ORR and OER performance of non-PGM catalysts, however, is more challenging due to the wide operational potential range. Diverse manganese oxides and perovskites possess promising bifunctional activity in alkaline media [4, 5, 20–29]. A major drawback in the implementation of these oxides in electrocatalyst layers is the inherently low electrical conductivity, 10^{-5}–10^{-6} S cm^{-1} and 2.3×10^{-1} S cm^{-1} for MnO_2 and $LaCoO_3$, respectively [25, 30], compared to 1.7×10^4 S cm^{-1} for IrO_2 [31]. To alleviate the low electrical conductivity, carbon-based materials are widely being used as catalyst supports or catalyst layer additives [4, 5, 14, 23, 28, 32, 33]. Carbons provide favorable characteristics including low cost ($0.95 USD per kg for carbon black), large BET surface area (e.g., approximately 200 m^2 g^{-1} for Vulcan XC-72 [34]), enhanced electrical conductivity (e.g., 2.7×10^{-1} S cm^{-1} for Vulcan XC-72 in loose powder form [34]) and good chemical stability in acidic and alkaline media [14, 35]. It was proposed that carbons with large fraction of meso-pores and thick crystalline walls generally provide higher electrical conductivity and better oxidation resistivity [36]. However, typical carbonaceous materials suffer durability issues mainly caused by carbon corrosion at the high anodic potentials corresponding to OER [14, 28, 37–43]. Carbon structure modifications such as graphitization or hetero-atom (e.g., S, P and N) doping can boost the durability to enhance their role as either catalyst support or even the ORR/OER bifunctional catalyst itself, mainly by increasing the defects and edge plan sites in the graphitic matrix [14, 28, 39, 44–46]. Zhang et al. reported high ORR/OER electrocatalytic activity and durability for mesoporous carbon foams co-doped with N and P in alkaline media, showing similar ORR electrocatalytic activity to commercial Pt/C catalyst as well as lower OER onset potential (up to 1700 mV$_{RHE}$) compared to Ru/C [44]. Using DFT calculations, they revealed that the most active sites for ORR and OER are N-dopant sites near the graphene edges and N/P co-doped graphene edges, respectively [44].

Nanostructured carbons such as carbon nanotubes, graphene and especially N-doped graphene, showed promising performances in oxygen electrodes either as catalyst support or as the ORR and OER electrocatalyst itself [14, 28, 47–51].

The aim of this research is to investigate graphene and N-doped graphene synthesized by the in situ simultaneous exfoliation method of Taheri and Gyenge [52, 53], alone or in combination with multi-walled carbon nanotubes (MWCNT) as either ORR/OER catalyst or as support for the highly active MnO_2–$LaCoO_3$ bifunctional catalyst developed by Hosseini and Gyenge [4, 5, 54]. It was shown that the combination of the two structurally different oxides, improves the ORR and OER bifunctional activity by a synergistic effect between the oxides compared to the individual components, as demonstrated also by the lower apparent Tafel slopes and higher exchange current densities for both ORR and OER in 6 M KOH [4, 54, 55]. To the best of authors' knowledge, a systematic study of combined graphene and MWCNT supports for non-PGM oxygen bifunctional catalysts, such as the manganese and perovskite oxides presented here, has not yet been reported in the literature.

2 Experimental section

2.1 Material preparation and characterization

Graphene and N-doped graphene microsheets have been produced using the method developed by Taheri and Gyenge using ionic liquid (IL)-assisted electrochemical exfoliation of graphite in aprotic solvents, and described extensively elsewhere [52]. Vulcan XC-72 was purchased from Cabot. γ-MnO_2 (reagent grade, ≥ 90%) and MWCNT (> 95%) were purchased from Sigma-Aldrich. The $LaCoO_3$ powder was synthesized via a co-precipitation method explained in our previous work [4]. The 50 wt% Pt on Graphitized Carbon was acquired from Tanaka Kikinzoku Kogyo K.K. in Japan.

Carbonaceous materials, MnO_2 and $LaCoO_3$ were studied by at least one of the following characterization methods: X-ray diffraction (XRD, D8 Advance Bruker diffractometer with a CuK$_{\alpha 1}$ source), field emission scanning electron microscopy (FESEM, Hitachi S-4700) and transmission electron microscopy (TEM, FEI Tecnai G2 200 kV). The operating conditions for XRD were as follows: generator set at 40 kV and 40 mA; Cu as X-ray source; wave length of 1.54439 Å K$_{\alpha 1}$; step size of 0.04° (2θ); step time of 230.4 s; range: between 5° and 90° for 2θ. For the XRD characterization experiments, powder samples of the oxides (about 1 g each) of the as-received (for the commercial MnO_2) or as-synthesized (for the perovskite oxide) were tested. Furthermore, about 5 mg of each powder (as-received or synthesized) was added to a double-sided carbon tape, which was applied on a SEM stub for subsequent characterization. Moreover, an 8-mm-in-diameter circular punch-cut of the

gas diffusion electrode (GDE) was attached to a double-sided carbon tape used to hold the sample on the SEM stub for microstructural analysis. For TEM studies, 10 mg of each powder was added to 5 ml of isopropyl alcohol (IPA) and sonicated for 15 min. Then, 10 µl of the ink was added to a TEM grid and left to dry for 1 h prior to testing.

Figure 1 presents the TEM images of carbonaceous materials as well as non-PGM oxides MnO_2 and $LaCoO_3$, used in this study. The microstructure of graphene consists of crumpled and randomly oriented larger-area graphene sheets together with small number of flakes with an average length of 200 nm (Fig. 1A). For N-doped graphene sample, the morphology is similar, with less flakes and more ultrathin graphene sheets (Fig. 1B). As for MWCNT, TEM micrographs show tangled tubes with outer diameter of 8–18 nm and length of 0.5–5 µm (Fig. 1C). The MnO_2 particles vary in shape from pillars with various length-to-width ratios to smooth spheres (Fig. 1D). For pillar-shaped particles, the length-to-width ratio changes from 3 to 7.5 with the lengths as small as 30 nm to max. 450 nm (Fig. 1D). The size of

sphere-like MnO_2 particles ranges from 70 to 100 nm in diameter. $LaCoO_3$ particle sizes are between 50 and 100 nm (Fig. 1E).

SEM images of the Sigma-Aldrich MnO_2 powder show agglomerates of pillar and sphere-like particles (Fig. 2A). The size range of these agglomerates was found to be between 0.5 and 3 µm. A flaky and porous morphology with sharp edges is observed for the synthesized $LaCoO_3$ powders using SEM analysis, forming agglomerates (Fig. 2B). Figure 2C presents a representative SEM micrograph of a mixed-oxide gas diffusion electrode studied here with MnO_2:$LaCoO_3$:Vulcan:Nafion:polytetrafluoroethylene (PTFE) (weight ratio of 1:1:1:0.6:0.6) as the catalyst layer, sprayed on a 40% PTFE-treated carbon cloth. Cross-sectional SEM images revealed a catalyst layer with an average thickness of about 25 µm. The XRD characterization of MnO_2 and $LaCoO_3$ is presented in the Fig. S1 and Table S1 (see supporting information).

2.2 Catalyst layer and gas diffusion electrode (GDE) preparation

To study the performance of the aforementioned carbonaceous materials as supports for MnO_2–$LaCoO_3$ (weight ratio of 1:1) or oxygen catalyst alone, a mixture of oxides (if present), carbonaceous material(s), IPA and 5 wt% Nafion solution was sonicated for 1 h. Next, a specified volume of the catalyst ink (5–15 µL) was drop-casted on a polished glassy carbon (GC) electrode to reach a loading of 0.5 mg cm^{-2} for the carbonaceous material(s) or oxides, whichever was present, and left in air to dry for another hour at 293 K. The final weight ratio of MnO_2 (if present):$LaCoO_3$ (if present):carbon(s):Nafion in the catalyst layer was 1:1:1:0.6.

Gas diffusion electrodes (GDEs) were fabricated using a CNC sprayer machine as follows. A catalyst ink of MnO_2, $LaCoO_3$, carbonaceous material, IPA, water, 5 wt% Nafion solution, and 60 wt% polytetrafluoroethylene (PTFE) suspension was sonicated for an hour and sprayed on a 4×4 cm (16 cm^2 geometric area) piece of 40 wt% PTFE-treated carbon cloth from Fuel Cell Earth Co., to achieve a loading of 0.5 mg cm^{-2} for MnO_2 and $LaCoO_3$ each. The MnO_2:IPA:water weight ratio was fixed at 1:50:16. The PTFE and dry Nafion contents of the catalyst layers were kept at 0.3 mg cm^{-2} each.

In all cases where more than one carbonaceous material was used, the loading of each carbon component was kept at 0.5 mg cm^{-2}.

2.3 Electrochemical measurements

A conventional three-electrode rotating disk electrode (RDE) half-cell setup was used for the electrochemical analysis of the catalysts. Two different types of working electrodes were
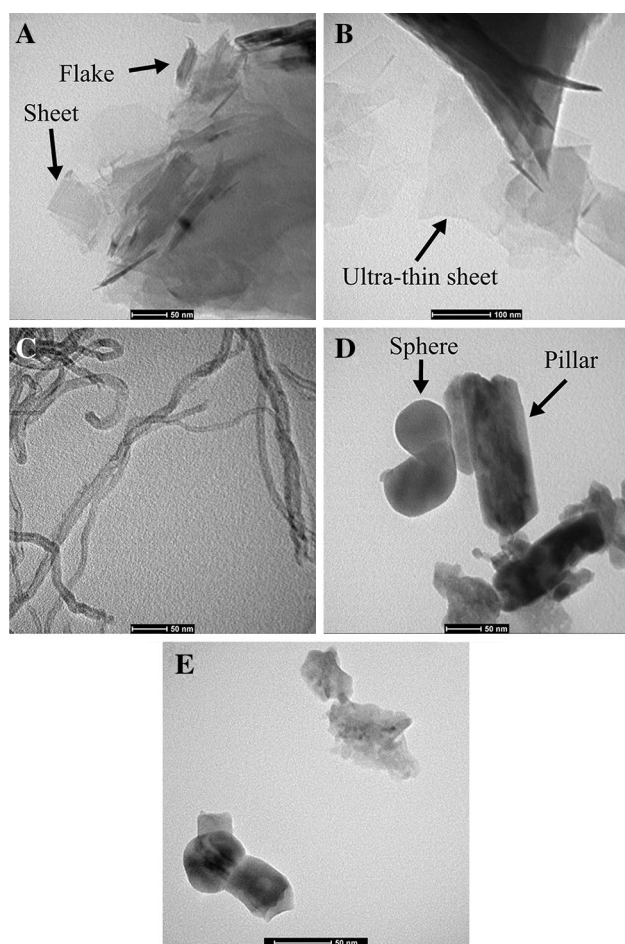

Fig. 1 TEM images of materials investigated in this study: **A** graphene, **B** N-doped graphene, **C** MWCNT, **D** MnO_2 and **E** $LaCoO_3$

Fig. 2 SEM images of **A** commercial Sigma-Aldrich MnO$_2$ powder (pillar and sphere-like particles are shown using dashed oval and circular shapes, respectively), **B** synthesized LaCoO$_3$ powder, and **C** a GDE consisting of MnO$_2$:LaCoO$_3$:Vulcan XC-72:Nafion:PTFE (weight ratio of 1:1:1:0.6:0.6) sprayed on a 40% PTFE-treated carbon cloth
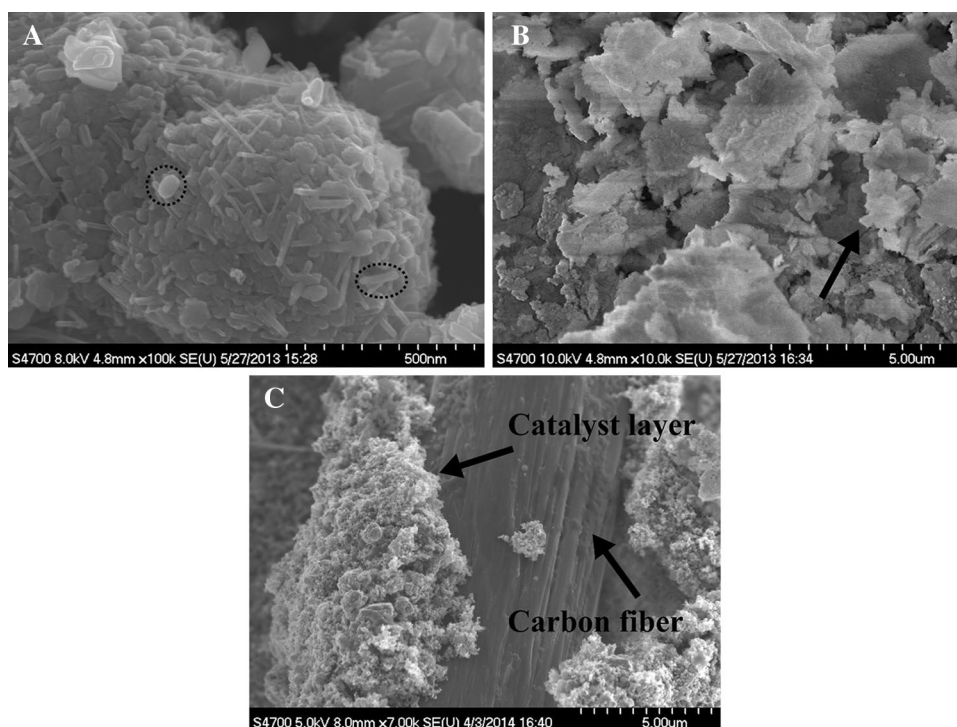
employed to test the electrocatalytic activity and durability of materials investigated here: (1) catalyst ink drop-casted on a 5-mm-in-diameter polished GC, (2) circular punch-cut 8-mm-in-diameter GDE fitted in a quick-fit exchangeable sample holder from radiometer analytical (#A35T450) with a geometric area of 0.283 cm^2 exposed to the electrolyte. The reference and counter electrodes were Hg/HgO/0.1 M KOH (MOE) from radiometer analytical (XR400) and platinum mesh, respectively.

There has been discussion in the community on the use Pt as counter electrode for electrocatalysis studies on non-PGM catalysts, focusing on the possibility of Pt dissolution and deposition on the non-PGM catalysts, which can affect the electrocatalytic activity of such materials. This issue is most significant for the hydrogen evolution reaction electrocatalysis, where due to the negative potentials (below 0 V$_{RHE}$) and possible high current densities on the working electrode, the Pt counter electrode can experience high anodic potentials causing Pt dissolution and re-deposition on the working electrode containing non-PGM catalyst. In addition, the electrolyte composition, counter vs. working electrode area ratio, temperature and experimentation time, can all effect, alone and in synergy, the rates of Pt dissolution and re-deposition. Therefore, replacement of Pt with carbon counter electrodes is recommended [55]. However, in the current study, focusing on the bifunctional ORR and OER electrocatalytic activity in alkaline media, using carbon as the counter electrode is not a good choice and high surface area Pt (e.g., mesh)

is preferred. During the OER cycle on the working electrode, if carbon is used as counter electrode, peroxide is also generated on the counter electrode by the two-electron ORR in alkaline media. The presence of peroxide in the electrolyte can interfere with the non-PGM catalyst on the working electrode and influence the measured current density during the ORR cycle. Furthermore, dependent on the source of carbon, transition metal impurities can be present such as Fe, Al, Mn, etc. Typically, the purity of the carbon counter electrode is not investigated and reported in most studies. These transition metals will easily dissolve under anodic conditions and could interfere with the oxygen electrochemistry on the working electrode. Other interfering effects could also result from carbon counter electrode corrosion such as CO generation [39, 41, 42].

Regarding the Pt mesh counter electrode employed here, it is also noted that the counter electrode never operated at very high anodic potentials; hence, the Pt dissolution rate was minimized. Furthermore, according to a study by the Jerkiewicz group [56], the surface area ratio of the working and counter electrodes ($A_{geom,WE}/A_{geom,CE}$) has a significant impact on the Pt counter electrode oxidation and dissolution. The lower the area ratio the lower is the Pt content in the electrolyte solution [56]. In the present case, this ratio is very small with a working electrode area of only 0.283 cm^2 and the Pt mesh area on the order of several hundred cm^2. Therefore, using extensive EDX, EELS and XRD analysis of our non-PGM electrodes we have never identified the presence of Pt on the working electrode.

The electrodes were connected to a computer-controlled VoltaLab 80 potentiostat and its associated RDE setup. The potential of the MOE reference electrode was 1073 mV versus RHE in 6 M KOH at 293 K measured using the reversible hydrogen reference electrode (HydroFlex) from Gaskatel GmbH. All potentials in this work are reported vs. RHE unless otherwise specified. The equilibrium oxygen electrode potential in 6 M KOH solution was calculated to be 1173 mV$_{RHE}$ or 100 mV$_{MOE}$ at 293 K. All measured currents are reported normalized by the geometric surface area of the electrodes (i.e., superficial current density).

To study the peroxide production efficiency, rotating ring disk electrode (RRDE) measurements were performed using a Pine RRDE electrode (AFE6R1GCPK) with a GC disk (5.7 mm in diameter) and ring (6.4 mm inner and 7.8 mm outer diameter) using linear sweep voltammetry (LSV) in O$_2$ saturated 6 M KOH at 293 K, starting with cathodic polarization from 1173 to 398 mV at 5 mV s^{-1} and various rotation speeds. The collection efficiency of the RRDE was 0.34 and the potential of the ring electrode was held at 1353 mV during the RRDE measurements.

To investigate the electrocatalytic activity of the catalysts, cyclic voltammetry (CV) tests up to one hundred successive potential cycles were performed in 6 M KOH between 673 and 1823 mV, starting with anodic polarization, at 5 mV s^{-1}, 293 K, 400 rpm. In some cases, a narrower potential range was used to avoid catalyst loss, especially for samples deposited on GC.

Prior to the reported electrocatalytic performance tests, each electrode was subjected to a break-in polarization protocol composed of five potential cycles in the same potential region as the following CV or LSV experiments. All cyclic and linear sweep voltammograms have been repeated for at least five times to ensure the reproducibility of the presented results. Moreover, all CV and LSV results are IR-drop corrected using the "Static Manual" ohmic drop compensation feature of the VoltaLab 80 potentiostat.

3 Results and discussion

3.1 ORR and OER behaviors of the catalyst layer supports: graphene, N-doped graphene, and MWCNT

First, the ORR and OER polarization behavior of graphene, N-doped graphene, and MWCNT alone and in combination was studied to establish the support contribution to the overall catalyst layer performance. The ORR kinetics is governed by the binding energies between the catalyst and oxygen containing intermediates, i.e., O$_2$$^-$, HO$_2$$^-$, and OH$^-$ [2, 14, 21, 43, 57]. Three mechanistic pathways are possible in alkaline media [2, 14, 43, 57–59]: (a) direct 4-electron pathway

(Eq. 1), (b) indirect 2×2 electron pathway with HO$_2$$^-$ intermediate (Eqs. 2 and 3) and (c) two-electron pathway with HO$_2$$^-$ product (Eq. 2). Pathways b) and c) cannot be totally separated as they strongly depend on the adsorption/desorption rate of HO$_2$$^-$, pH and the applied potential.

$$O_2 + 2H_2O + 4e^- \rightarrow 4OH^- \left(E^\circ_{298} = 1227 \text{ mV vs. RHE}\right) \tag{1}$$

$$O_2 + H_2O + 2e^- \rightarrow HO_2^- + OH^- \left(E^\circ_{298} = 750 \text{ mV vs. RHE}\right) \tag{2}$$

$$HO_2^- + H_2O + 2e^- \rightarrow 3OH^- \left(E^\circ_{298} = 1704 \text{ mV vs. RHE}\right) \tag{3}$$
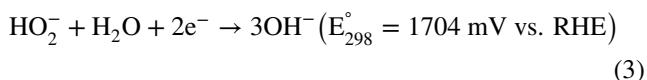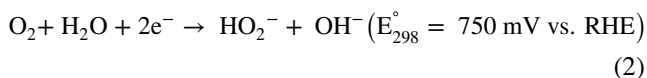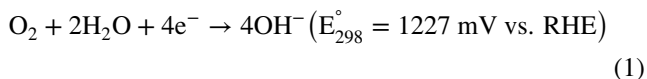
$$2HO_2^- \rightarrow 2OH^- + O_2 \tag{4}$$

Figure 3 presents the ORR polarization curves obtained on a RDE for graphene, N-doped graphene and MWCNT used as supports in GDEs. For reference, the ORR polarization on Vulcan XC-72 is also included. The carbon loadings were 0.5 mg cm^{-2} in all cases. The peak reduction currents between 700 and 830 mV versus RHE are due to the two-electron reduction of O$_2$–HO$_2$$^-$ (Eq. 2), whereas at lower potentials HO$_2$$^-$ reduction to OH$^-$ takes place (Eq. 3). These results are consistent with the 2×2-electron reduction pathway of adsorbed O$_2$ [60–62]. Many studies reported a mixture of 2 and 4 electron pathways for MWCNT, graphene and N-doped graphene [28, 43, 44, 63, 64]. The edges of N-doped graphene are believed to provide activity toward ORR via the four-electron reduction pathway [65]. Depending on the N-doping structure at the edge sites, the doped nitrogen can help promote adsorption of oxygen on the adjacent carbon sites, facilitating the formation of ORR intermediates [65, 66].
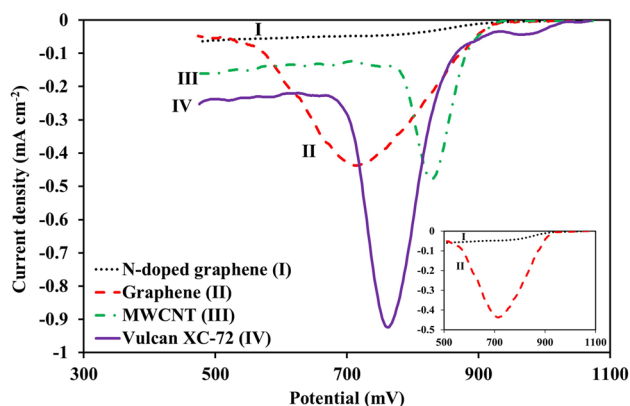

Fig. 3 RDE results for ORR on N-doped graphene (I), Graphene (II), MWCNT (III), and Vulcan XC-72 (IV). Carbon loadings of 0.5 mg cm^{-2} each. O$_2$ saturated 6 M KOH. 5 mV s^{-1}. 293 K. 400 rpm. The inset shows the ORR polarization curves for graphene and N-doped graphene

Compared to the commonly employed carbon black Vulcan XC-72, the ORR electrode kinetics on either graphene or N-doped graphene is more sluggish as shown by the up to 65 mV lower ORR onset potential and smaller reduction currents (Fig. 3). From the perspective of electrocatalyst support application, the slower rate of HO_2^- production on the graphene-based supports is an advantage compared to Vulcan XC-72 in metal–air batteries and fuel cells because accumulation of HO_2^- can be detrimental to the long term membrane and electrode durability.

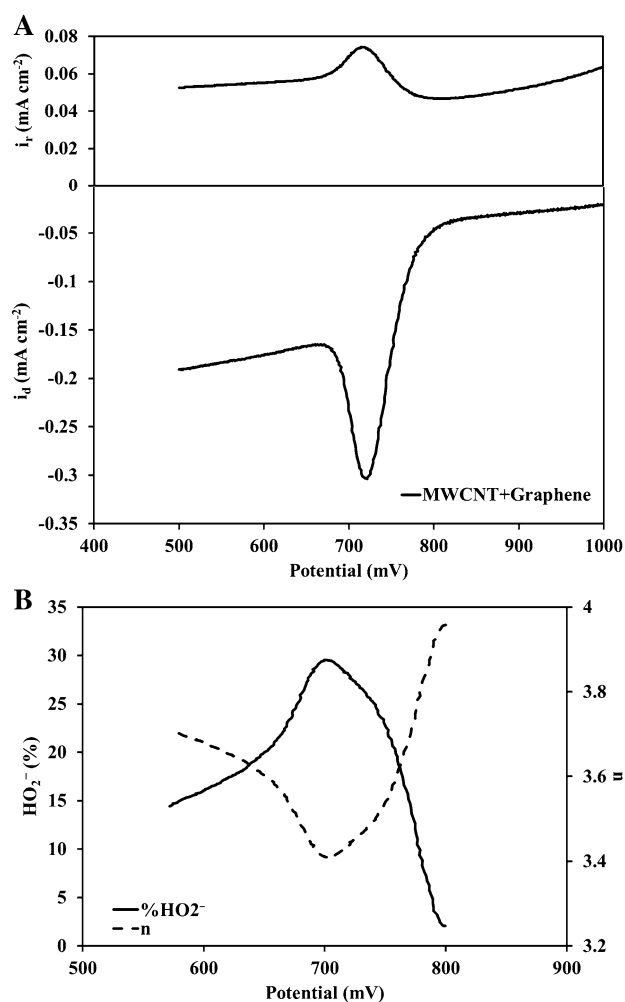Figure 4 presents the RRDE results for ORR on the hybrid support composed of MWCNT and graphene in a 1:1 weight ratio. The hybrid support shows a reduction peak corresponding to ORR at around 720 mV, following a mixture of 2 and 4 electron pathways with a maximum HO_2^- production yield of 30% at 720 mV (Fig. 4). Even though the addition of MWCNT to graphene can help increase the electro-active surface area of the graphene support, the ORR onset potential and peak reduction current density values show low activity for ORR compared to other ORR electrocatalysts such as MnO_2 [55, 67, 68].

The polarization curves in the OER potential region of the carbon supports, alone or in combination, are shown by Fig. 5. Vulcan XC-72 generated the highest anodic current density of about 1 mA cm^{-2} at 1600 mV, which is due mainly to OER but also with contributions from carbon corrosion [41, 42]. For comparison, the oxidation current densities at 1600 mV on graphene and N-doped graphene were approximately 20 and 150 times lower, respectively (Fig. 5). Carbon corrosion occurs mainly through two processes: (1) dissolution to carbonate ion (CO_3^{2-}) and (2) gasification to carbon monoxide [41, 42]. The rates of these processes are dependent on the carbon synthesis and treatment methods and the presence of diverse catalysts [39, 41, 42, 64]. In the present case, N-doped graphene followed by graphene have the lowest activity for corrosion and OER.

For the hybrid support composed of either graphene or N-doped graphene mixed with MWCNT, the oxidation current densities at potentials above 1500 mV are higher than for the individual components (Fig. 5). This enhancement is mainly due to the 3D scaffold-like architecture created with the graphene sheets and the MWCNT rods/coils. This arrangement increases the effective electroactive surface area exposed to the electrolyte as compared to the
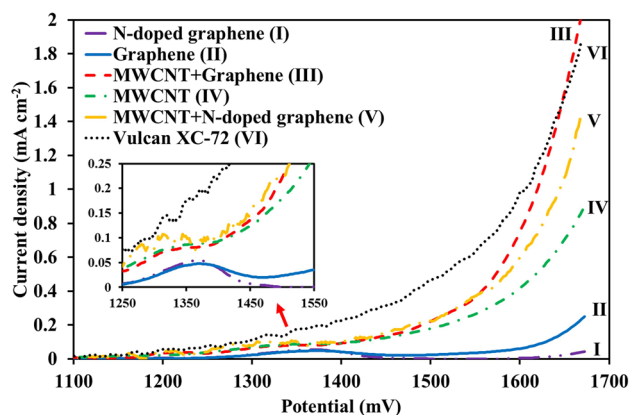

Fig. 4 RRDE results for ORR on MWCNT+Graphene (1:1 weight ratio). **A** O_2 reduction current densities on the disk electrode (i_d) (Bottom), the corresponding oxidation current densities on the ring at 1353 mV (i_r) as a function of disk potentials (Top). **B** Calculated percentage of hydrogen peroxide produced (%HO_2^-) and number of electrons transferred per O_2 molecule (n). Carbon loadings of 0.5 mg cm^{-2} each. O_2 saturated 6 M KOH. 5 mV s^{-1}. 293 K. 1600 rpm

Fig. 5 OER potential region of the bifunctional ORR/OER performance of carbonaceous materials, i.e., Graphene, N-doped graphene, MWCNT, Vulcan XC-72, MWCNT+Graphene and MWCNT+N-doped graphene. Initial stage, IR-corrected polarization curves obtained by potential scanning between 475 and 1673 mV. Carbon loadings 0.5 mg cm^{-2}, each. For cases where two materials were mixed, a weight ratio of 1:1 was used. Cycle number five is reported in all cases. O_2-saturated 6 M KOH. 293 K. 400 rpm. 5 mV s^{-1}

tightly stacked 2D graphene morphology in the absence of MWCNT.

3.2 Support effect on the ORR/OER bifunctional electrocatalytic activity of MnO$_2$–LaCoO$_3$

Figures 6 and 7 present the OER/ORR cyclic voltammograms in O$_2$ saturated 6 M KOH of the mixed oxide MnO$_2$–LaCoO$_3$ (1:1 weight ratio) catalyst in combination with six supports: graphene, N-doped graphene (Fig. 6A), MWCNT, Vulcan XC-72 (Fig. 6B), MWCNT+graphene and MWCNT+N-doped graphene (Fig. 7).

The mixed oxide catalyst was selected based on extensive investigations performed by us previously [55, 67]. The ORR and OER current densities were approximately an order of magnitude smaller with individual graphene-based supports compared to either Vulcan or MWCNT (Fig. 6). The compact stacking of the graphene micro sheets creates a dense, low porosity catalyst layer with low effective catalytic area
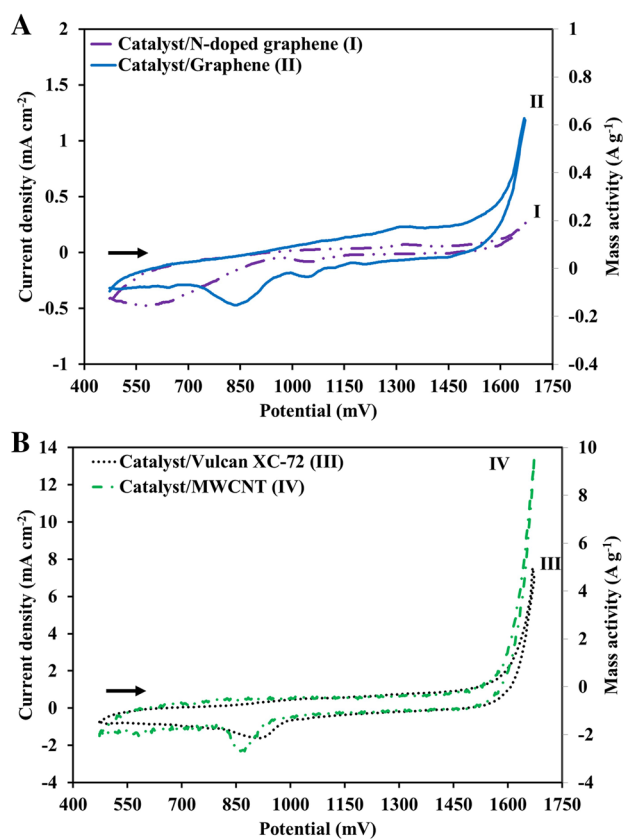
Fig. 7 Bifunctional ORR/OER performance of MnO$_2$–LaCoO$_3$ with hybrid supports: MWCNT+Graphene and MWCNT+N-doped graphene. Total oxide and total carbon loadings: 0.5 mg cm^{-2}, each. Weight ratio: 1:1:1:1 for MnO$_2$:LaCoO$_3$:Carbon1:Carbon2. Cycle number five is reported in all cases. The total mass of oxides and carbons are used to calculate the mass activity of each sample. Other conditions idem to Fig. 5
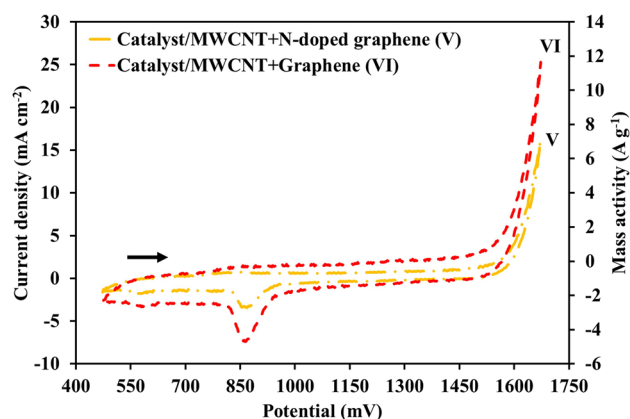
[69]. However, when graphene is combined with MWCNT a hybrid support is formed, which is synergistically enhancing the effective ORR and OER activity of MnO$_2$–LaCoO$_3$ catalyst (Fig. 7). Thus, with graphene+MWCNT support the superficial current densities at 850 mV (for ORR) and 1650 mV (for OER), were between two to three times higher compared to the MWCNT support alone and over an order of magnitude higher than for the graphene support alone (Figs. 6, 7). At a benchmark current density of 10 mA cm^{-2}, the OER overpotentials for MnO$_2$–LaCoO$_3$ were as follows: 442 mV with MWCNT+graphene and 471 mV with MWCNT+N-doped graphene. Furthermore, for comparison, the mass activities under identical conditions for a 50% Pt/graphitized carbon catalyst were as follows: ORR: -2 A g^{-1} (at 850 mV) and OER: 3.9 A g^{-1} (at 1650 mV) (Fig. S2).

The enhanced bifunctional activities with the hybrid supports are due to two complementary effects, catalyst layer morphology and support-catalyst interaction, respectively. In case of the MWCNT+graphene hybrid, the graphene microsheets separated by MWCNT pillars create a structured 3D scaffold catalyst layer architecture that increases the effective electroactive surface area compared to the catalyst layer containing individually either graphene or MWCNT. Regarding the catalyst-support interaction, DFT studies showed that the constant difference between the binding energies of HOO*$_{(ads)}$ and HO*$_{(ads)}$ intermediates on many metals, their oxides and even carbon materials such as graphenes, is a major factor causing high ORR and OER overpotentials [44, 70–75]. Breaking away from this linear scaling relationship via modification of catalyst surfaces including introduction of defects, applying magnetic fields or manipulating catalyst-support interactions could lower the ORR and

Fig. 6 Bifunctional ORR/OER performance of MnO$_2$–LaCoO$_3$ catalyst supported on various carbonaceous materials. **A** Graphene and N-doped graphene, **B** MWCNT and Vulcan XC-72. The oxides and carbon loadings were 0.5 mg cm^{-2}, each. A weight ratio of 1:1:1 for MnO$_2$:LaCoO$_3$:Carbon was used. Cycle number five is reported in all cases. The total mass of oxides and carbon are used to calculate the mass activity of each sample. Other conditions idem to Fig. 5

OER overpotentials [32, 55]. Hence, it is hypothesized that there could be interaction effects between MnO_2–$LaCoO_3$ and the hybrid support MWCNT+graphene (or N-doped graphene) that could assist in breaking the scaling relationship between the $HOO^*_{(ads)}$ and $HO^*_{(ads)}$ binding energies. Further in-depth studies are needed to explore and test the validity of this hypothesis.

When analyzing the oxidation current densities on MnO_2–$LaCoO_3$, there are two other additional oxidation reactions that could also contribute to the measured anodic currents: (i) carbon corrosion (as discussed in the previous section), and (ii) MnO_2 oxidation (referred to also as MnO_2 corrosion) (Eq. 5):

$$MnO_2 + 4OH^- \rightarrow MnO_4^- + 2H_2O + 3e^- \left(E_{298}^{\circ} = 1421 \text{ mV vs. RHE} \right) \tag{5}$$
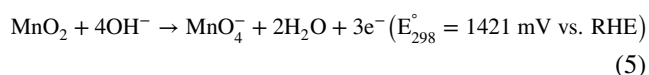
It was shown that the rate of carbon corrosion processes on catalyzed or un-catalyzed carbons in concentrated alkaline solutions decrease dramatically above specific anodic potentials (e.g., above 1600 mV in 30 wt% KOH at 318 K) [41]. Thermodynamics indicates that the second possible corrosion reaction at potentials greater than 1421 mV is the MnO_2 oxidation to MnO_4^- (Eq. 5). Kinetically, however, the rate of this reaction is a function of the electrolyte composition and concentration, as well as anodic potential. Nevertheless, it has been shown that at potentials higher than 1900 mV, the MnO_2 oxidation current is virtually zero in 0.5 M KOH [76]. Gao et al. argued that this could be due to the formation of a passivating oxide layer without further negative effect on the OER electrocatalytic activity of manganese oxide [76].

The Tafel plots associated with the various MnO_2–$LaCoO_3$ catalyst layers (Fig. 5) showed apparent ORR and OER Tafel slopes between -52 and -86 mV dec^{-1} and 83 and 127 mV dec^{-1}, respectively (Fig. S3 and Table S2). The apparent exchange current densities for MnO_2–$LaCoO_3$/MWCNT+graphene and MnO_2–$LaCoO_3$/MWCNT+N-doped graphene catalyst layers were 2.1 and 0.33 μA cm^{-2}, respectively. The latter values are 16 and 1000 times, respectively, higher than the exchange current densities for the individual graphene-based materials (Table S2).

3.3 The support effect on bifunctional accelerated degradation

Figure 8 shows accelerated degradation results for the bifunctional activity of GDE catalyst layers composed of MnO_2–$LaCoO_3$ and two supports, MWCNT+graphene and Vulcan XC-72, respectively. The electrodes were subjected to 100 cycles between 673 and 1873 mV vs. RHE with a sweep rate of 5 mV s^{-1} for a total testing time of 48,000 s. Figure 8 reports the superficial current densities at 800 mV (for ORR) and 1750 mV (for OER), respectively.
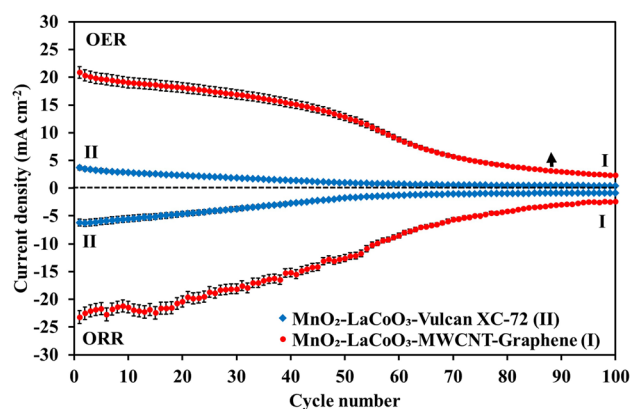

Fig. 8 ORR (bottom) and OER (top) current densities at 800 mV and 1750 mV vs. RHE during 100 successive potential cycling between 673 and 1873 mV using MnO_2–$LaCoO_3$/MWCNT+Graphene (weight ratios: 1:1:1:1) and MnO_2–$LaCoO_3$/Vulcan XC-72 (weight ratios: 1:1:1) GDEs, respectively. The oxide and carbon loadings were 0.5 mg cm^{-2} each on a 40 wt% PTFE-treated carbon cloth substrate. Other conditions idem to Fig. 5

The hybrid support induced superior activity for the mixed oxide electrocatalyst compared to Vulcan XC-72 (Fig. 8). Thus, the OER current density ratio between the catalyst layer with hybrid support and Vulcan XC-72 was 5.7 for the 1st cycle and 5.1 after 100 cycles. Similarly, the ORR current density ratio between the hybrid and Vulcan XC-72 supported mixed oxide catalyst layers were as follows: 3.8 for the 1st cycle and 2.8 after 100 cycles.

For the MnO_2 catalysts, the loss of activity with deep potential cycling between the OER and ORR regions is due to phase changes, modification of defects and oxygen vacancy concentrations and gradual formation and build-up of low catalytic activity oxides and oxyhydroxides such as MnO, MnOOH [4, 12, 20–22, 55, 58, 59, 77, 78]. These changes in the MnO_2 structure will affect the $HOO^*_{(ads)}$/ $HO^*_{(ads)}$ binding energies as major contributors to ORR/ OER overpotentials on oxide surfaces [32, 70–72, 79–83].

The perovskite component of the catalyst $LaCoO_3$ is known to be stable in the OER region but on its own it has a very low ORR activity compared to manganese oxides [4, 55, 80, 84, 85]. However, the potential cycling stability of $LaCoO_3$ alone or in combination with other oxides between the ORR and OER regions was much less investigated. Previously, we have shown that the mixed oxide MnO_2–$LaCoO_3$ catalyst can suffer more severe bifunctional electrocatalytic performance degradation than MnO_2 alone [67]. Furthermore, we also demonstrated that the activity can be recovered by potassium ion intercalation [55, 67]. Therefore, the interfacial interactions of $LaCoO_3$ with the other components of the catalyst layer, such as MnO_2 and carbons, during severe potential cycling should be taken into account. In our future work in this area,

further characterizations will be performed to examine the complex interactions among the catalyst layer components: MnO_2, $LaCoO_3$, graphene, and MWCNT.

4 Conclusions

The effect of catalyst support on the ORR and OER electrocatalytic activity and durability of MnO_2–$LaCoO_3$ catalyst was investigated in 6 M KOH, 293 K. Graphene and N-doped graphene, prepared by ionic liquid assisted simultaneous electro-exfoliation of iso-molded graphite electrodes, were studied as supports alone or in combination with MWCNT. Graphene and N-doped graphene are advantageous as supports compared to the commonly employed Vulcan XC-72 due to their superior corrosion stability in the OER region and lower rate of HO_2^- formation in the ORR potential region. However, MnO_2–$LaCoO_3$ catalyst layers with only graphene-based supports performed poorly in terms of both OER and ORR activity. The dense stacking of the graphene microsheets decreases the effective catalytic area and catalyst layer utilization.

The hybrid support composed of graphene combined with MWCNT in a 1:1 weight ratio produced catalyst layers with excellent bifunctional ORR and OER activities. Thus, the overpotential at 10 mA cm^{-2} for MnO_2–$LaCoO_3$ with hybrid support was 442 mV, compared to 625 mV with the Vulcan XC-72 support. These values compare favorably with literature results, such as 500 mV for Co_3O_4, 510 mV for $NiFe_2O_4$, 550 mV for $LaCoO_3$, 500 mV for MnO_2, and 430 mV for NiO at 10 mA cm^{-2} [86]. Regarding ORR as well, the catalyst mass activity with the hybrid support at 850 mV is about four times the one for Vulcan XC-72. The effectiveness of the hybrid support is attributed to the 3D scaffold-like architecture composed of flat microsheets (graphene) separated by pillars (MWCNT). The 3D catalyst layer architecture enhances the utilization efficiency, thereby, increasing the effective catalytic area and activity.

Furthermore, accelerated degradation experiments comprised of 100 successive potential cycles between the 673 and 1873 mV versus RHE for a total of over 13 h of testing, also confirmed the superior bifunctional activity of the MnO_2–$LaCoO_3$ with the hybrid support compared to the reference Vulcan XC-72.

References

1. Lee J, Jeong B, Ocon JD (2013) Curr Appl Phys 13:309
2. Ludwig J (2006) J Power Sources 155:23
3. Grdeń M, Alsabet M, Jerkiewicz G (2012) ACS Appl Mater Interfaces 4:3012
4. Benhangi PH, Alfantazi A, Gyenge E (2014) Electrochim Acta 123:42
5. Stern L-A, Hu X (2014) Faraday Discuss 176:363
6. Serov A, Aziznia A, Benhangi PH et al (2013) J Mater Chem A 1:14384
7. Blizanac BB, Ross PN, Marković NM (2006) J Phys Chem B 110:4735
8. Lee WH, Kim H (2011) Catal Commun 12:408
9. Gorlin Y, Jaramillo TF (2010) J Am Chem Soc 132:13612
10. Lee Y, Suntivich J, May KJ et al (2012) J Phys Chem Lett 3:399
11. Marković NM, Ross PN (1994) J Electrochem Soc 141:2590
12. Pickrahn KL, Park SW, Gorlin Y et al (2012) Adv Energy Mater 2:1269
13. Jaouen F, Proietti E, Lefevre M et al (2011) Energy Environ Sci 4:114
14. Cheng F, Chen J (2012) Chem Soc Rev 41:2172
15. Gutsche C, Moeller CJ, Knipper M et al (2016) J Phys Chem C 120:1137
16. Ahmed J, Mao Y (2016) Electrochim Acta 212:686
17. Shao M, Chang Q, Dodelet J-P, Chenitz R (2016) Chem Rev 116:3594
18. Sahraie NR, Kramm UI, Steinberg J et al (2015) Nat Commun 6:8618
19. Zhan Y, Lu M, Yang S et al (2016) ChemCatChem 8:372
20. Chabre Y, Pannetier J (1995) Prog Solid State Ch 23:1
21. Gyenge EL, Drillet J-F (2012) J Electrochem Soc 159:F23
22. Gorlin Y, Lassalle-Kaiser B, Benck JD et al (2013) J Am Chem Soc 135:8525
23. Stoerzinger KA, Risch M, Han B, Shao-Horn Y (2015) ACS Catal 5:6021
24. Bockris JO, Otagawa T (1983) J Phys Chem 87:2960
25. Bockris JOM, Otagawa T (1984) J Electrochem Soc 131:290
26. Bockris JOM, Otagawa T, Young V (1983) J Electroanal Chem 150:633
27. Suntivich J, May KJ, Gasteiger HA et al (2011) Science 334:1383
28. Cao R, Lee J-S, Liu M, Cho J (2012) Adv Energy Mater 2:816
29. Lu ZY, Wang HT, Kong DS et al (2014) Nat Commun 5:4345
30. Lang X, Hirata A, Fujita T, Chen M (2011) Nat Nano 6:232
31. Rogers DB, Shannon RD, Sleight AW, Gillson JL (1969) Inorg Chem 8:841
32. Gupta S, Kellogg W, Xu H et al (2016) Chem—An Asian J 11:10
33. Hardin WG, Slanac DA, Wang X et al (2013) J Phys Chem Lett 4:1254
34. Dehkhoda AM, Ellis N, Gyenge E (2014) J Appl Electrochem 44:141
35. Shao Y, Liu J, Wang Y, Lin Y (2009) J Mater Chem 19:46
36. Banham D, Feng F, Fürstenhaupt T et al (2011) J Power Sources 196:5438
37. Ng JWD, Tang M, Jaramillo TF (2014) Energy Environm Sci 7:2017
38. Müller S, Striebel K, Haas O (1994) Electrochim Acta 39:1661
39. Ross PN, Sattler M (1988) J Electrochem Soc 135:1464
40. Pettersson J, Ramsey B, Harrison D (2006) J Power Sources 157:28

41. Ross PN, Sokol H (1984) J Electrochem Soc 131:1742
42. Staud N, Ross PN (1986) J Electrochem Soc 133:1079
43. Ge X, Sumboja A, Wuu D et al (2015) ACS Catal 5:4643
44. Zhang J, Zhao Z, Xia Z, Dai L (2015) Nat Nanotechnol 10:444
45. Bao X, von Deak D, Biddinger EJ et al (2010) Chem Commun 46:8621
46. Choi CH, Park SH, Woo SI (2011) Green Chem 13:406
47. Zhang S, Shao Y, Yin G, Lin Y (2010) J Mater Chem 20:2826
48. Liu R, Li S, Yu X et al (2011) J Mater Chem 21:14917
49. Fujigaya T, Uchinoumi T, Kaneko K, Nakashima N (2011) Chem Commun 47:6843
50. Li Y, Dai H (2014) Chem Soc Rev 43:5257
51. Ye D, Wu T, Cao H et al (2015) RSC Adv 5:26710
52. Najafabadi AT, Gyenge E (2014) Carbon 71:58
53. Taheri Najafabadi A, Gyenge E (2015) Carbon 84:449
54. Gyenge E, Hosseini-Benhangi P (Filed on August 30, 2016) An oxygen electrode and a method of manufacturing the same. U.S. (15/251,267) and Canadian (2,940,921) patent applications
55. Hosseini-Benhangi P, Garcia-Contreras MA, Alfantazi A, Gyenge EL (2015) J Electrochem Soc 162:F1356
56. Tian M, Cousins C, Beauchemin D et al (2016) ACS Catal 6:5108
57. Vielstich WL, A; Gasteiger, Hubert A (eds) (2003) Fuel cell electrocatalysis. Handbook of fuel cells: fundamentals, technology, and applications. Wiley, New Jersey
58. Lima FHB, Calegaro ML, Ticianelli EA (2006) J Electroanal Chem 590:152
59. Lima FHB, Calegaro ML, Ticianelli EA (2007) Electrochim Acta 52:3732
60. Li X, Qu W, Zhang J, Wang H (2011) J Electrochem Soc 158:A597
61. Sunarso J, Torriero AAJ, Zhou W et al (2012) J Phys Chem C 116:5827
62. Jiang J, Yi B (2005) J Electroanal Chem 577:107
63. Tian G-L, Zhao M-Q, Yu D et al (2014) Small 10:2251
64. Wang Z-L, Xu D, Xu J-J, Zhang X-B (2014) Chem Soc Rev 43:7746
65. Bao X, Nie X, von Deak D et al (2013) Top Catal 56:1623
66. Vazquez-Arenas J, Galano A, Lee DU et al (2016) J Mater Chem A 4:976
67. Hosseini-Benhangi P, Alfantazi A, Gyenge E (2014) Electrochim Acta 123:42
68. Hosseini-Benhangi P, Kung CH, Alfantazi A, Gyenge EL (2017) ACS Appl Mater Interfaces 9:26771
69. Najafabadi AT, Leeuwner MJ, Wilkinson DP, Gyenge EL (2016) ChemSusChem 9:1689
70. Man IC, Su H-Y, Calle-Vallejo F et al (2011) ChemCatChem 3:1159
71. Koper MTM (2011) J Electroanal Chem 660:254
72. Su H-Y, Gorlin Y, Man IC et al (2012) Phys Chem Chem Phys 14:14010
73. Zhang J, Xia Z, Dai L (2015) Sci Adv 1:e1500564
74. Jiao Y, Zheng Y, Jaroniec M, Qiao SZ (2014) J Am Chem Soc 136:4394
75. Li M, Zhang L, Xu Q et al (2014) J Catal 314:66
76. Gao Q, Ranjan C, Pavlovic Z et al (2015) ACS Catal 5:7265
77. Kozawa A, Kalnoki-Kis T, Yeager JF (1966) J Electrochem Soc 113:405
78. Ruetschi P (1976) J Electrochem Soc 123:495
79. Chen C-F, King G, Dickerson RM et al (2015) Nano Energy 13:423
80. May KJ, Carlton CE, Stoerzinger KA et al (2012) J Phys Chem Lett 3:3264
81. Li L, Feng X, Nie Y et al (2015) ACS Catal 5:4825
82. Suntivich J, Gasteiger HA, Yabuuchi N et al (2011) Nat Chem 3:546
83. Mueller DN, Machala ML, Bluhm H, Chueh WC (2015) Nat Commun 6:6097
84. Poux T, Napolskiy FS, Dintzer T et al (2012) Catal Today 189:83
85. Hong WT, Risch M, Stoerzinger KA et al (2015) Energy Environ Sci 8:1404
86. Jung S, McCrory CCL, Ferrer IM et al (2016) J Mater Chem A 4:3068

Affiliations

Miguel A. Garcia-Contreras[1,2] · Pooya Hosseini-Benhangi[1,3] · Előd L. Gyenge[1]

✉ Előd L. Gyenge
elod.gyenge@ubc.ca

Miguel A. Garcia-Contreras
miguel.garcia@inin.gob.mx

Pooya Hosseini-Benhangi
pooya.hosseini@ubc.ca

[1] Department of Chemical and Biological Engineering & Clean Energy Research Center (CERC), The University of British Columbia, 2360 East Mall, Vancouver, BC V6T 1Z3, Canada

[2] Department of Chemistry, National Institute of Nuclear Research, Carretera México-Toluca s/n, 52750 La Marquesa Ocoyoacac, Estado De México, Mexico

[3] Department of Materials Engineering, The University of British Columbia, 6350 Stores Road, Vancouver, BC V6T 1Z4, Canada